Coherent multidimensional spectroscopy in polariton systems

Daniela Gallego-Valencia,[1,2,3,*] Lars Mewes,[4,†] Johannes Feist,[2,3,‡] and José Luis Sanz-Vicario[1,§]

[1]*Grupo de Física Atómica y Molecular, Instituto de Física, Universidad de Antioquia, 050010 Medellín, Colombia*

[2]*Departamento de Física Teórica de la Materia Condensada, Universidad Autónoma de Madrid, 28049 Madrid, Spain*

[3]*Condensed Matter Physics Center (IFIMAC), Universidad Autónoma de Madrid, 28049 Madrid, Spain*

[4]*Technische Universität München, TUM School of Natural Sciences, Fakultät für Chemie, Lichtenbergstraße 4, 85748 Garching, Germany*

(Received 22 November 2023; accepted 16 May 2024; published 11 June 2024)

The fast dynamics of molecular polaritonics is scrutinized theoretically through the implementation of two-dimensional spectroscopy protocols. We derive conceptually simple and computationally efficient formulas to calculate two-dimensional spectra for molecules, each of them modeled as a system of two electronic states including vibrational relaxation, immersed in an optical cavity, thus coupled to quantized radiation. Cavity photon losses and molecular relaxation are incorporated into the Hamiltonian dynamics to form an open quantum system that is solved through a master equation. In the collective case, the relaxation dynamics into dark states is revealed to be the crucial factor to explain the asymmetries in both the diagonal and cross peaks of two-dimensional spectra for long waiting times between excitation and detection, a feature shown by recent experiments. Our theoretical method provides a deeper insight in those processes that yield relevant signals in multidimensional molecular spectroscopy.

DOI: 10.1103/PhysRevA.109.063704

I. INTRODUCTION

Aggregates of organic molecules subject to confined electromagnetic fields in extended cavities provide a test bed to understand the interplay between excitons, vibrations and phonons, and photons in physics. Excitations in these collective systems produce entangled quasiparticles (polaritons) that inherit properties from both matter and light [1–4]. The fast inner workings of these complex systems in the short time domain are still far from being fully understood. To unveil the polariton dynamics of these systems, ultrafast laser techniques based on pump-probe principles can be applied. Coherent multidimensional spectroscopy (CMDS) provides insight into the vibronic structure and ultrafast dynamics of molecular systems upon optical excitation [5–11]. CMDS yields correlated signals between the frequencies of absorption and those of detection, which allows for a deeper understanding of the fast excitation, emission, and relaxation mechanisms of the system. CMDS has already provided remarkable new insights into photophysics and photochemistry [12,13] since it allows a direct spectroscopic observation of couplings, system-bath interactions, and energy relaxation within microscopic systems. Two-dimensional infrared (2D-IR) spectroscopy and two-dimensional electronic spectroscopy (2DES) are of particular relevance and reveal insightful details about polaritonic systems under vibrational [14–16] and electronic [17] strong coupling, respectively.

Model Hamiltonians in quantum optics have been quite successful to describe the fundamental physics behind photon-matter interactions, from quantum Rabi to Jaynes-Cummings (JC) models in the case of a single emitter [18,19], to Dicke and Tavis-Cummings (TC) models for a collection of emitters [20–22].

In this article, we theoretically study and analyze CMDS of organic molecule polaritons under electronic strong coupling. For the sake of completeness and clarity, we first study the prototypical JC case of a single emitter and then extend the description to the TC case with multiple molecules. Inspired by the asymmetric signals observed in recent CMDS experiments involving molecular J-aggregates immersed in optical cavities [23], we study the 2DES signals derived from an open quantum system consisting of a TC Hamiltonian with N identical emitters, each described by two electronic states subject to dissipative and relaxation processes induced by vibrational modes. Our model is expected to apply to an ensemble of dye molecules with a weak exciton-phonon coupling characterized by small Huang-Rhys factors and Stokes shifts, so that the coupling to molecular vibrations can be treated perturbatively. In particular, molecular J-aggregates form delocalized collective electronic states, whose coupling to vibrational modes is weak [24,25]. The polariton photodynamics of a TC model has also been investigated recently in connection with pump-probe spectroscopies [26]. Other recent works on 2DES using the quantum stochastic Liouville equation [27,28] or the Heisenberg-Langevin model [29] are of interest.

The paper is organized as follows. The theoretical framework is explained in Sec. II, where we review some aspects of the polariton structure of JC and TC models relevant for our study. Since we deal with an open quantum system, the

*Contact author: daniela.gallegov@udea.edu.co
†Contact author: lars.mewes@tum.de
‡Contact author: johannes.feist@udea.edu.co
§Contact author: jose.sanz@udea.edu.co

master equation is solved using the Liouvillian superoperator. We describe the representation of the Liouvillian matrix and the distribution of its complex eigenvalues and give a comprehensive account of the routes to calculate linear (absorption and emission) and especially the nonlinear multidimensional spectroscopic signals, arriving at a remarkably simple formula expressing these signals using the eigenstate of the Liouvillian.

Our results are presented in Sec. III–first, the linear spectra, which already show asymmetry in the absorption and emission of the lower and upper electronic polaritons. We give a detailed survey on the successive steps that build up the asymmetries in 2DS (two dimensional spectroscopy), the separate role of populations and coherences in the nonlinear spectra, the partial components contributing to the 2DS according to the Feynman paths, and the changes in the spectra as the number of molecular emitters increases. We finally use our method to reproduce the main features of 2DS obtained in recent experiments with molecular J-aggregates within optical microcavities. In Sec. IV we present our conclusions and some future perspectives.

II. THEORETICAL FRAMEWORK

A. Hamiltonian and master equations

The Tavis-Cummings model for N identical two-level emitters interacting with a single-cavity mode is described by the following Hamiltonian (with the case $N = 1$ corresponding to the Jaynes-Cummings model):

$$\hat{H} = \hbar\omega_c \hat{a}^\dagger \hat{a} + \hbar\omega_0 \sum_{i=1}^{N} \hat{\sigma}_i^\dagger \hat{\sigma}_i + \hbar g \sum_{i=1}^{N} (\hat{a}^\dagger \hat{\sigma}_i + \hat{\sigma}_i^\dagger \hat{a}), \quad (1)$$

in terms of the photon creation (annihilation) operator $\hat{a}^\dagger$ ($\hat{a}$) and the excitation (deexcitation) operator $\hat{\sigma}_i^\dagger$ ($\hat{\sigma}_i$) of molecule i. The emitters with natural frequency ω_0 interact with a single-mode cavity radiation with frequency ω_c (with a detuning $\Delta = \omega_c - \omega_0$) that leads to an energy splitting $\Omega_R = \sqrt{4Ng^2 + \Delta^2}$ (called the Rabi splitting in the case $\Delta = 0$). When comparing results with different numbers of emitters N below, we scale g so as to maintain Ng^2 and thus Ω_R constant.

Two-dimensional spectroscopy within a perturbative regime involves states in the lowest excitation manifolds Λ_0, Λ_1, and Λ_2, where the subscript denotes the number of excitations in the system. A general diagram of the polariton energy levels of the JC Hamiltonian for one emitter and TC Hamiltonian for $N > 2$ emitters in resonance, $\omega_c = \omega_0$, is shown in Fig. 1. In both cases, the zero-excitation manifold contains a single state, the ground state $|G\rangle$. For the JC Hamiltonian, in Fig. 1(a), all other excitation manifolds Λ_n contain two states, a lower $|L_n\rangle$ and an upper $|U_n\rangle$ polariton with Rabi splitting $\omega_{U_nL_n} \equiv \omega_{U_n} - \omega_{L_n} = \sqrt{n}\Omega_R$ (for simplicity, we drop the n subindices for $n = 1$) that increase with excitation number n (commonly called the vacuum Rabi splitting for $n = 1$). The dominant radiative transitions for external driving of the system are indicated with red double arrows in the figure. Blue single arrows indicate the transitions induced by dissipative processes, with cavity photon losses indicated by solid lines (these are the same transitions that are accessible by external driving, i.e., the solid blue and red arrows are the same) and vibrational relaxation between polaritons mediated by molecular dephasing-type interactions indicated by blue dashed lines (which only occur between states within a given excitation manifold). In Fig. 1(b), we show a scheme of energy levels for a TC Hamiltonian with N emitters. The first excitation manifold Λ_1 consists of lower $|L\rangle$ and upper $|U\rangle$ states, separated by the Rabi frequency Ω_R and $N - 1$ degenerate dark states $|D\rangle$. The second excitation manifold Λ_2 has four energy levels: lower $|L_2\rangle$ and upper $|U_2\rangle$ polaritons plus $N - 1$ degenerate states $|A_2\rangle$ and $N - 1$ degenerate states $|B_2\rangle$, along with $N(N - 3)/2 + 1$ degenerate states $|M_2\rangle$. For the case $N = 2$, the states A_2 and B_2 are degenerate and the states M_2 disappear. The definitions for the vertical arrows are identical to Fig. 1(a). In the limit $N \to \infty$, the TC model becomes linear, i.e., the collection of identical emitters behaves like a harmonic oscillator [22], and the system is then described by normal modes (independent harmonic oscillators) [30]. The n-excitation energy levels can then be understood as corresponding to the excitation of n independent quasiparticles (e.g., for $n = 2$: two lower polaritons, or two upper polaritons, or one lower polariton and one dark exciton, etc.). For $N \gg n$, this is still a useful picture even when N is finite, with small energy shifts that can be interpreted as interactions between the quasiparticles.

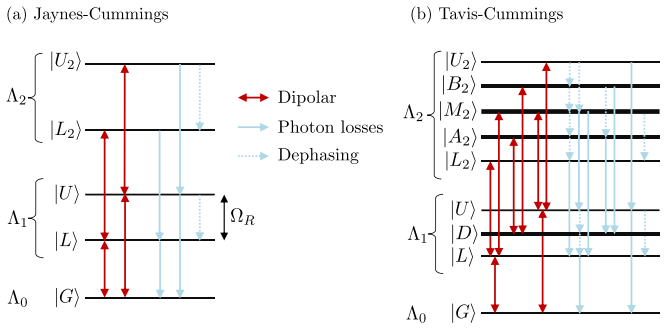

FIG. 1. Scheme of energy levels and dominant transitions for (a) the Jaynes-Cummings Hamiltonian with one emitter and (b) the Tavis-Cummings Hamiltonian with $N > 2$ emitters.

We assume that the polariton system is embedded within an environment that produces incoherent dynamics, in particular photon losses from the cavity. We also treat the internal vibrational modes of the molecules (and their coupling to vibrations and phonons in the host material) as an effective bath with a dephasing-type interaction. The open quantum system is then treated under the Markovian approximation [31–33]. Thus, the dynamics of the system density matrix is governed by a Liouville master equation $\dot{\hat{\rho}}(t) = \hat{\mathcal{L}}[\hat{\rho}(t)]$, where the Liouvillian superoperator is given by

$$\hat{\mathcal{L}}[\hat{\rho}(t)] = -\frac{i}{\hbar}[\hat{H}, \hat{\rho}(t)] + \kappa \hat{L}_{\hat{a}}[\hat{\rho}(y)] + \sum_i \hat{\Gamma}_{\hat{\sigma}_i^\dagger \hat{\sigma}_i}[\hat{\rho}(t)], \quad (2)$$

with a standard Lindblad term $\hat{L}_{\hat{a}}$ for the cavity losses with decay rate κ (lifetime $1/\kappa$)

$$\hat{L}_{\hat{a}}[\hat{\rho}(t)] = \hat{a}\hat{\rho}(t)\hat{a}^\dagger - \tfrac{1}{2}\{\hat{a}^\dagger \hat{a}, \hat{\rho}(t)\}. \quad (3)$$

The vibrational bath is described through a Markovian Bloch-Redfield-Wangsness (BRW) superoperator $\hat{\Gamma}_{\hat{O}}$ for a single

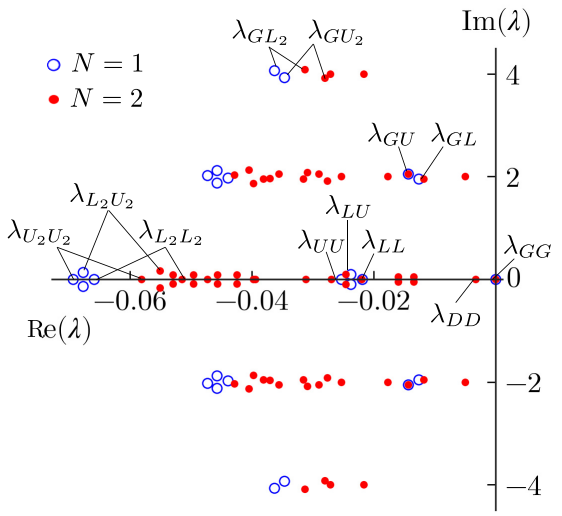

FIG. 2. Location of the Liouvillian eigenvalues $\lambda_{\alpha\beta} = -\Gamma_{\alpha\beta} - i\omega_{\alpha\beta}$ in the complex plane for the open Jaynes-Cummings model (blue open circles) and the open Tavis-Cummings model for $N = 2$ emitters (red circles). In both cases, $\omega_c = \omega_e = 2$ eV and $\hbar\Omega_R = 0.1$ eV. Cavity lifetime is 15 fs ($\hbar\kappa = 44$ meV) and molecular relaxation time is 50 fs ($\hbar\gamma = 13$ meV). The real part Re[λ] is related to the total decay width (to all final channels) and the imaginary part Im[λ] to energy differences between any two Hamiltonian eigenstates. The most relevant eigenvalues corresponding to populations $\lambda_{\Lambda_i\Lambda_i}$ and coherences $\lambda_{\Lambda_i\Lambda_j}$ and the latter only when $\Lambda_1 \leqslant \Lambda_2$ (for the opposite they are complex conjugated) are indicated in the plot.

emitter in the form

$$\hat{\Gamma}_{\hat{O}}[\hat{\rho}(t)] = -\frac{1}{\hbar^2}\sum_{m,n}\{\hat{O}_{mn}[\hat{O}, |m\rangle\langle n|\hat{\rho}(t)]S_B(\omega_{mn}) + \text{H.c.}\} \tag{4}$$

expressed in the Hamiltonian eigenbasis $\{|n\rangle\}$ [31,34]. It is worth noting that the usual secular approximation is not implemented in this work while (Lamb) energy shifts are neglected. The BRW formalism describes the system-bath interaction induced by the molecular dephasing-type operators $\hat{\sigma}_i^\dagger\hat{\sigma}_i$, which mediate vibrational relaxation between the polaritons [35]. The bath (assumed independent for each molecule) is characterized by the noise power spectrum

$$S_B(\omega) = \begin{cases} (1 + n(\omega))J(\omega) & \omega \geqslant 0 \\ n(-\omega)J(-\omega) & \omega < 0 \end{cases}, \tag{5}$$

where $n(\omega) = 1/(e^{\hbar\omega/k_BT} - 1)$ is the Bose-Einstein thermal population and $J(\omega)$ the spectral density of the bath. In the following, we treat two cases: (1) a simplified model at zero temperature, where $n(\omega) = 0$ and the spectral density $J(\omega) = \gamma$ is constant, and (2) a more realistic model at finite temperature with a spectral density of Debye form, $J(\omega) = 2\gamma\delta\omega/(\omega^2 + \delta^2)$, with a molecular relaxation rate γ and a cutoff parameter δ.

B. Liouvillian eigenvalues and eigenstates

The master equation, Eq. 2, describes the evolution of the density matrix in the presence of dissipative terms. The

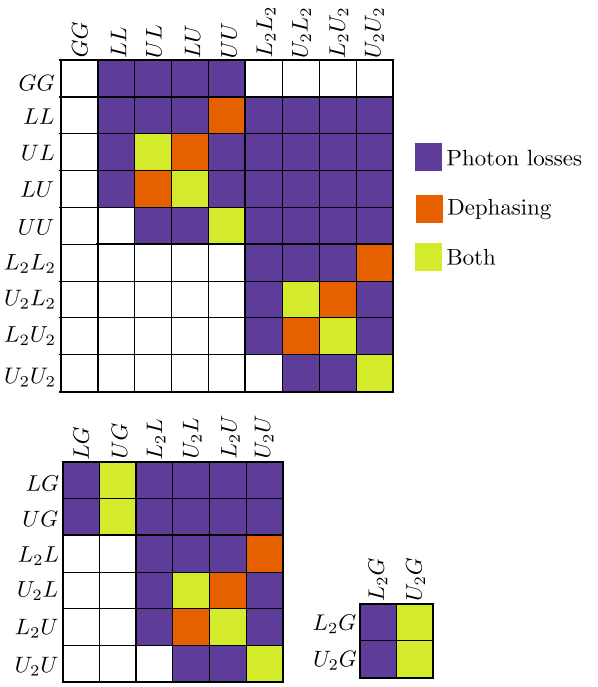

FIG. 3. Scheme for the structure of the Liouvillian (25 × 25) matrix with elements $\mathcal{L}_{\Lambda_i,\Lambda_j;\Lambda_k\Lambda_\ell}$ represented in terms of the Hamiltonian basis set of the Jaynes-Cummings model up to the second excitation manifold $\{G, L, U, L_2, U_2\}$. The full matrix is organized as five independent block matrices (the second 6 × 6 and third 2 × 2 block matrices in the figure must be accompanied with their respective complex conjugates). Colored grids correspond to nonzero matrix elements. Colors inside each grid indicate the incoherent mechanism contributing to the element: photon loss with purple (dark gray) dephasing type with orange (medium gray) or both of them with green (light gray).

Liouvillian superoperator is not Hermitian and thus has complex eigenvalues. The density operator can be represented in the Hilbert space basis, $\hat{\rho} = \sum_{\alpha\beta}\rho_{\alpha\beta}|\alpha\rangle\langle\beta|$, with a dimension $\dim_H^2$, where $\dim_H$ is the dimension of the Hilbert space. The Liouvillian superoperator is then an object with four indices, $\mathcal{L}_{\alpha\beta;\alpha'\beta'}$, but can be interpreted as a matrix in the Liouville space basis, whose elements $|\alpha\beta\rangle\rangle$ map directly to the corresponding Hilbert space operators $|\alpha\rangle\langle\beta|$. The Liouvillian matrix representation thus has dimension $\dim_H^2 \times \dim_H^2$. When it is diagonalizable, $\hat{\mathcal{L}}$ is characterized by its (complex) eigenvalues λ_i as well as its right and left eigenvectors, $|v_i\rangle\rangle$ and $\langle\langle v_i|$, with $\langle\langle v_i|v_j\rangle\rangle = \delta_{ij}$. Often, the imaginary part of λ_i is very close to an energy difference between two eigenstates $|\alpha\rangle$ and $|\beta\rangle$ of the Hamiltonian, and the corresponding eigenvalues of $\hat{\mathcal{L}}$ can be approximately labeled as

$$\lambda_{\alpha\beta} = -\Gamma_{\alpha\beta} - i(\omega_{\alpha\beta} + \pi_{\alpha\beta}), \tag{6}$$

where $\omega_{\alpha\beta} = (E_\alpha - E_\beta)/\hbar$ corresponds to the energy difference between the two eigenstates and $\pi_{\alpha\beta}$ is a small shift. For the case $\alpha = \beta$, both $\omega_{\alpha\beta}$ and $\pi_{\alpha\beta}$ are zero and the Liouvillian eigenvalues are real. In that case, the identification in terms of state labels can be performed by inspection of the expansion coefficients of the Liouvillian eigenstates.

In Fig. 2, we show the Liouvillian eigenvalues and corresponding state labels (up to the second excitation manifold) of the JC model (five states) and the TC model for $N = 2$ emitters (eight states), with 25 and 64 Liouvillian eigenvalues, respectively. Eigenvalues corresponding to population dynamics $\lambda_{\alpha\alpha}$ lie along the real axis, while those corresponding to coherences $\lambda_{\alpha\beta}$ have nonzero imaginary parts. Notice that the real parts of λ for $N = 1$ effectively act as lower and upper bounds for decay widths of polariton systems with $N > 1$ (except for the presence of new dark states and their coherences), thus indicating in general a nonlinear scaling of decays for higher excitation manifolds as N increases. For the real eigenvalues, one can observe a hierarchy in the total population decay rates, $0 = \Gamma_{GG} < \Gamma_{LL} < \Gamma_{UU} < \Gamma_{L_2L_2} < \Gamma_{U_2U_2}$. The fastest decay corresponds to the highest energy level $|U_2\rangle$ due to the large number of available decay channels (both photonic and vibrational). It is worth noting that coherences also decay along with populations.

The structure of the Liouvillian matrix (which is the generator of the dissipative dynamics) also reflects the asymmetry in the different decay processes. In Fig. 3, we include a colored scheme of the Liouvillian matrix for the JC model indicating those matrix elements responsible for either photon losses or vibrational relaxation or both simultaneously. The matrix is block diagonal, such that each block evolves in time independently. The first matrix block contains elements with the form $(\Lambda_i\Lambda_i; \Lambda_j\Lambda_j)$ for $i, j = 0, 1, 2$ (note that labels $\Lambda_0 = \{G\}$, $\Lambda_1 = \{L, U\}$, $\Lambda_2 = \{L_2, U_2\}$ correspond to excitation manifolds). There are transitions $\Lambda_i\Lambda_i \to \Lambda_{i-1}\Lambda_{i-1}$ due to photon losses, while the opposite process (pumping) $\Lambda_i\Lambda_i \to \Lambda_{i+1}\Lambda_{i+1}$ does not occur. Similarly, within the second block, the photon losses show up in transitions between coherences $\Lambda_2\Lambda_1 \to \Lambda_1\Lambda_0$, but not in the opposite direction. Molecular vibrational relaxation is present only within the blocks $(\Lambda_i\Lambda_i; \Lambda_i\Lambda_i)$ with $i = 1, 2$, $(\Lambda_{i+1}\Lambda_i; \Lambda_{i+1}\Lambda_i)$ with $i = 0, 1$, and $(\Lambda_{i+2}\Lambda_i; \Lambda_{i+2}\Lambda_i)$ with $i = 0$.

While the Liouvillian matrix elements may be calculated in closed form, the dynamics $\hat{\rho}(t) = e^{\hat{\mathcal{L}}t}\hat{\rho}(0)$ must be solved numerically. As an example, we discuss an initial state that is a superposition of polaritons within the first excitation manifold, i.e., $\hat{\rho}(0) = |\Psi\rangle\langle\Psi|$ with $|\Psi\rangle = C_L|L\rangle + C_U|U\rangle$. The evolution is then fully determined by the zero- and one-excitation manifolds, and the reduced Liouvillian master equation takes the form

$$\frac{\mathrm{d}}{\mathrm{d}t}\begin{pmatrix}\rho_{GG}(t)\\ \rho_{LL}(t)\\ \rho_{UL}(t)\\ \rho_{LU}(t)\\ \rho_{UU}(t)\end{pmatrix} = \begin{pmatrix}0 & \kappa/2 & \kappa/2 & \kappa/2 & \kappa/2\\ 0 & -\kappa/2 & -\kappa/4 & -\kappa/4 & \gamma/4\\ 0 & -\kappa/4 & -\kappa/2-\gamma/8-i\Omega_R & \gamma/8 & -\kappa/4\\ 0 & -\kappa/4 & \gamma/8 & -\kappa/2-\gamma/8+i\Omega_R & -\kappa/4\\ 0 & 0 & -\kappa/4 & -\kappa/4 & -\kappa/2-\gamma/4\end{pmatrix}\begin{pmatrix}\rho_{GG}(t)\\ \rho_{LL}(t)\\ \rho_{UL}(t)\\ \rho_{LU}(t)\\ \rho_{UU}(t)\end{pmatrix}. \tag{7}$$

Of the five eigenvalues of this Liouvillian matrix, two have simple analytic forms, $\lambda_{GG} = 0$, $\lambda_{UU} = -\kappa/2 - \gamma/4$, while the remaining three, λ_{LL}, λ_{LU}, λ_{UL}, are the analytic solutions of the polynomial $256\kappa\Omega_R^2 + (16\gamma\kappa + 32\kappa^2 + 64\omega_R^2)\lambda + (2\gamma + 12\kappa)\lambda^2 + \lambda^3 = 0$. These solutions can be approximated as $\lambda_{LL} \approx -\kappa/2$, $\lambda_{LU} \approx -\kappa/2 - \gamma/8 + i\tilde{\Omega}_R$ and $\lambda_{UL} \approx -\kappa/2 - \gamma/8 - i\tilde{\Omega}_R$, with a shifted Rabi frequency $\tilde{\Omega}_R = \omega_{UL} + \pi_{UL}$ (see also Fig. 2 to locate these relevant eigenvalues). Time propagation is straightforward within the diagonalized (spectral) representation of the Liouvillian, with populations given by $\rho_{\alpha\alpha}(t) = \sum_{\alpha'\beta'} C^{\alpha\alpha}_{\alpha'\beta'} e^{\lambda_{\alpha'\beta'}t}$, where $C^{\alpha\alpha}_{\alpha'\beta'} = \langle\langle *|\alpha\alpha\rangle\rangle v_{\alpha'\beta'}\langle\langle *|v_{\alpha'\beta'}\rangle\rangle\hat{\rho}(0)$. In particular, the populations for the above-mentioned initial condition can be written as

$$\rho_{\alpha\alpha}(t) = C^{\alpha\alpha}_{LL}e^{-\Gamma_{LL}t} + C^{\alpha\alpha}_{UU}e^{-\Gamma_{UU}t} + 2e^{-\Gamma_{UL}t}\Re\left[C^{\alpha\alpha}_{UL}e^{i\tilde{\Omega}_R t}\right], \tag{8}$$

where we have used that $C^{\alpha\alpha}_{UL} = (C^{\alpha\alpha}_{LU})^*$. Eq. 8 involves two terms with exponential decays for Liouvillian eigenstates associated with populations, for the $|v_{LL}\rangle\rangle$ and $|v_{UU}\rangle\rangle$ components, and additional damped oscillatory terms due to the Liouvillian coherences $|v_{LU}\rangle\rangle$ and $|v_{UL}\rangle\rangle$. As shown below, this result qualitatively explains the behavior of the diagonal and cross peaks in 2D spectra after excitation, with respect to the waiting time delay, namely, exponential decay accompanied by Rabi oscillations.

The TC model with $N = 2$ emitters adds a new dark state D in the dynamics and the master equation now involves a 6×6 reduced Liouvillian matrix as shown in Eq. 9. One realizes that while photon loss rates enter in TC in analogy with the JC model, the vibrational relaxation rates enter differently and not only in the new column and row involving the dark state. Thus, the presence of dark states modifies the global dynamics of populations and coherences within the whole system.

$$\frac{\mathrm{d}}{\mathrm{d}t}\begin{pmatrix}\rho_{GG}(t)\\ \rho_{LL}(t)\\ \rho_{UL}(t)\\ \rho_{DD}(t)\\ \rho_{LU}(t)\\ \rho_{UU}(t)\end{pmatrix} = \begin{pmatrix}0 & \kappa/2 & \kappa/2 & 0 & \kappa/2 & \kappa/2\\ 0 & -\kappa/2 & -\kappa/4+\gamma/8 & \gamma/4 & -\kappa/4+\gamma/8 & \gamma/8\\ 0 & -\kappa/4 & -\kappa/2-3\gamma/16-i\Omega_R & -\gamma/8 & \gamma/16 & -\kappa/4+\gamma/8\\ 0 & 0 & -\gamma/8 & -\gamma/4 & -\gamma/8 & \gamma/4\\ 0 & -\kappa/4 & \gamma/16 & -\gamma/8 & -\kappa/2-\gamma/8+i\Omega_R & -\kappa/4+\gamma/8\\ 0 & 0 & -\kappa/4 & 0 & -\kappa/4 & -\kappa/2-3\gamma/8\end{pmatrix}\begin{pmatrix}\rho_{GG}(t)\\ \rho_{LL}(t)\\ \rho_{UL}(t)\\ \rho_{DD}(t)\\ \rho_{LU}(t)\\ \rho_{UU}(t)\end{pmatrix} \tag{9}$$

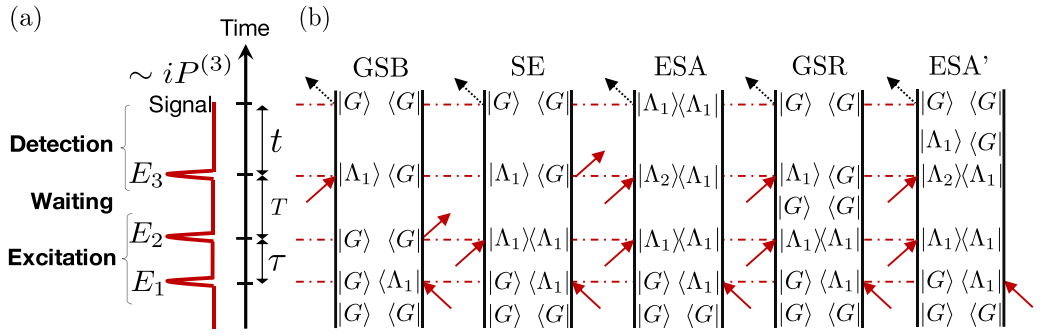

FIG. 4. (a) 2DS scheme showing three delayed laser pulses separated by coherence time τ and waiting time T. The signal is emitted during the detection time t. (b) Set of double-sided Feynman diagrams for the rephasing phase-matching condition $(-k_1 + k_2 + k_3)$ considering the excitation manifolds $\{\Lambda_0, \Lambda_1, \Lambda_2\}$, that correspond to GSB, SE, and ESA processes, plus those GSR and ESA′ processes derived when relaxation occurs after excitation. Red arrows indicate dipole interactions with the laser pulses and outgoing black dotted arrows represent the detected signal. Note that the notation $|\Lambda_1\rangle\langle\Lambda_1|$ indicates both populations and coherences, since $\Lambda_1 = L, U$.

The Liouvillian real eigenvalues of the JC model corresponding to the decay widths Γ have a dependence upon the choice of rate parameters κ (photon loss) and γ (vibrational relaxation). The decay widths show a linear scaling with κ, with a slope $\frac{2n-1}{2}$ for each excitation manifold Λ_n, and remain with the same trend for any number of molecular emitters N. Widths also display a linear scaling against the relaxation rate γ with slopes that depend on the nature of the state more than on the excitation manifold. For instance, in the JC model, λ_{LL} and $\lambda_{L_2L_2}$ share zero, λ_{UU} and $\lambda_{U_2U_2}$ share the same $\gamma/4$, and coherences λ_{LU} and λ_{UL} have $\gamma/8$. However, the molecular relaxation has a more complex scaling rule when N increases.

C. Linear absorption and emission spectra

Absorption and linear emission spectroscopy characterize the linear response of the system upon excitation. For absorption, the spectra is obtained as the Fourier transform of the two-time correlation function

$$S_{\mathrm{Abs}}(\omega_L) = \Re\left[\int_0^\infty \langle \hat{a}(t')\hat{a}^\dagger(0)\rangle e^{i\omega_L t'} \mathrm{d}t'\right]. \tag{10}$$

Note that in Fabry-Perot-like cavities the laser pumping through the mirrors is treated following the input-output theory, where the external laser pulses only drive the cavity mode(s) directly, which in turn mediate the coupling to the molecules [36]. Emission is obtained from the response under excitation by a weak continuous-wave laser driving field with frequency ω_L, i.e., $\hat{H}_L(t) = E_0(\hat{a}e^{i\omega_L t} + \hat{a}^\dagger e^{-i\omega_L t})$, described within the rotating-wave approximation. Transforming to a rotating frame with the unitary operator $U(t) = e^{i\hat{a}^\dagger \hat{a}\omega_L t/\hbar}$ yields a time-independent Hamiltonian without affecting the other terms in the Liouvillian superoperator. The emission spectra can then be calculated from another two-time correlation function in the steady state s (fulfilling $\dot{\rho} = 0$), i.e.,

$$S_{\mathrm{Em}}(\omega_L, \omega) = \Re\left[\int_0^\infty \langle \hat{a}^\dagger(t')\hat{a}(0)\rangle_s e^{-i\omega t'} \mathrm{d}t'\right]. \tag{11}$$

Note that the correlation does not disappear for $t \to \infty$, but reaches a constant value, $\lim_{t\to\infty}\langle \hat{a}^\dagger(t)\hat{a}(0)\rangle_s = |\langle \hat{a}\rangle_s|^2$, corresponding to elastic scattering of the laser, i.e., a delta peak at frequency ω_L. This contribution is not plotted in the emission spectra shown below.

D. Non-linear two-dimensional spectroscopy

While linear spectroscopies only involve the two lowest excitation manifolds (Λ_0, Λ_1), 2D spectroscopy to lowest order involves the three lowest excitation manifolds $(\Lambda_0, \Lambda_1, \Lambda_2)$, and can be understood as a coherent excitation energy-resolved pump-probe experiment. As depicted in Fig. 4(a), the first interaction of the system with the field $E_1(t)$ creates a coherence that evolves according to the Liouvillian during the coherence time delay τ. The interaction with $E_2(t)$ converts the initial coherence into a population on the ground or excited state. The system evolves during the waiting time T before a third field interaction with $E_3(t)$ generates a coherence that eventually radiates a signal field during the detection time period t, which is proportional to the third-order polarization $P^{(3)}(\tau, T, t)$.

Two common routes to compute third-order spectra are to either directly use third-order perturbation theory [37–39] or to extract the third-order component of the density matrix from the full nonperturbative solution of the quantum dynamic equations [40,41]. We follow the first route here, which provides a conceptually simple way to understand the underlying physics. The third-order polarizability is thus given by $P^{(3)}(t) = \mathrm{Tr}[\hat{\mu}\ \rho^{(3)}]$, where $\rho^{(3)}$ corresponds to the third-order perturbative component of the density matrix, and $\hat{\mu}$ is the operator coupling the system to the incoming laser.

$\rho^{(3)}$ can be expressed via time-ordered integrals, where the initial density operator ρ_0 is subject to three laser interactions at the times $t_1 < t_2 < t_3$:

$$\rho^{(3)}(t) = \int_{t_0}^{t} \mathrm{d}t_3 \int_{t_0}^{t_3} \mathrm{d}t_2 \int_{t_0}^{t_2} \mathrm{d}t_1 \mathcal{G}(t - t_3)\check{V}(t_3)\mathcal{G}(t_3 - t_2) \times \check{V}(t_2)\mathcal{G}(t_2 - t_1)\check{V}(t_1)\rho(t_0). \tag{12}$$

Here, the notation $\check{V}(t)$ indicates a superoperator that applies the interaction operator $\hat{V}(t) = -\hat{\mu}E(t)$ as a commutator, $\check{V}(t)\rho(t) = \frac{1}{i\hbar}[\hat{V}(t), \rho(t)]$, with $E(t)$ as the driving laser field amplitude, while $\mathcal{G}(\Delta t) = e^{\mathcal{L}\Delta t}$ indicates the field-free time propagator (Green's function) over a time interval Δt. The

third-order polarization can be reexpressed in terms of the third-order response function $S(t, T, \tau)$ (being t, T, and τ general time intervals) as

$$P^{(3)}(t_f) = \int_{t_0}^{t_f} \mathrm{d}t_3 \int_{t_0}^{t_3} \mathrm{d}t_2 \int_{t_0}^{t_2} \mathrm{d}t_1 \times E(t_3)E(t_2)E(t_1)S(t_f - t_3, t_3 - t_2, t_2 - t_1), \tag{13}$$

where

$$S(t, T, \tau) = \mathrm{Tr}[\hat{\mu}\mathcal{G}(t)\breve{\mu}\mathcal{G}(T)\breve{\mu}\mathcal{G}(\tau)\breve{\mu}\rho(t_0)]. \tag{14}$$

We now assume the sudden impulsive limit for the laser fields involved, with a Dirac delta as the envelope function for the three laser fields $E(t) = E^0\delta(t - \tau_i)\exp[i(\pm k_i r \mp \omega_i t)]$, for $i = 1, 2, 3$ (note that here E^0 has dimensions of electric field by time). This is a reasonable approximation for sufficiently short nonoverlapping laser pulses. It implies a large spectral bandwidth and produces simplified expressions since it gives $P^{(3)}(t_f) = S(t, T, \tau)$, where now $t = t_f - \tau_3$, $T = \tau_3 - \tau_2$, and $\tau = \tau_2 - \tau_1$. For target systems that conserve momentum (as planar Fabry-Pérot cavities do in the in-plane directions), phase-matching conditions imply that the signal can be split into distinct components for which emission occurs in different directions that can be distinguished experimentally [39]. The most typical choices are the *rephasing* (R) $(-k_1 + k_2 + k_3)$ and *nonrephasing* (NR) $(+k_1 - k_2 + k_3)$ components, since the sum of both contributions produces the total absorptive 2DS. The chosen sign + or − for k_i in the phase-matching condition determines (within the rotating-wave approximation) whether the excitation $\hat{\mu}^+$ or deexcitation $\hat{\mu}^-$ part of the coupling operator acts for each interaction. For instance, the response function for the rephasing matching condition reads

$$S_R(t, T, \tau) = \mathrm{Tr}[\hat{\mu}^-\mathcal{G}(t)\breve{\mu}^+\mathcal{G}(T)\breve{\mu}^+\mathcal{G}(\tau)\breve{\mu}^-\rho(t_0)]. \tag{15}$$

Here, the last operator $\hat{\mu}^-$ corresponds to the signal emission. By expanding the nested commutators, one arrives at eight terms, each of them corresponding to a particular double-sided Feynman diagram of the rephasing process. Under coherent evolution of the system and within the rotating-wave approximation, only three out of eight diagrams contribute to the signal, namely, ground-state bleaching (GSB), stimulated emission (SE), and excited state absorption (ESA), as included in Fig. 4(b). Taking into account incoherent processes such as relaxation (which are often orders of magnitude faster in polaritonic systems than in isolated molecules), the system does not stay in the same eigenstate even during the field-free evolution, and additional Feynman diagrams become relevant. Note that the Feynman diagrams shown in Fig. 4(b) are based on labels corresponding to excitation manifolds, not explicit states, such that relaxation processes that occur within an excitation manifold are implicitly contained in each one. One additional path, the ground-state recovery (GSR), involves population relaxation from the first excitation manifold, i.e., $|\Lambda_1\rangle\langle\Lambda_1| \to |G\rangle\langle G|$, and ensures that the GSB signal decays when the molecular system relaxes back into the ground state (see Ref. [42]). Another path, ESA′, is equivalent to ESA but with an additional decay process happening between excitation by the third pulse and photon emission t, i.e., $|\Lambda_2\rangle\langle\Lambda_1| \to |\Lambda_1\rangle\langle G|$. We find this pathway relevant in the buildup of the 2DS at short T. Note that both GSR and ESA′ paths involve relaxation due to decay of cavity photons, thus connecting different excitation manifolds. Vibrational relaxation only happens within the same excitation manifold.

The rephasing 2D spectrum $S_R(\omega_t, T, \omega_\tau)$ is obtained after the 2D Fourier transform of $S_R(t, T, \tau)$, while the total absorptive 2D spectrum is obtained by adding also the nonrephasing contribution, $S_{\mathrm{Abs}}(\omega_t, T, \omega_\tau) = \Re(S_R + S_{NR})$.

E. Simple formula for 2DS

Here, we derive a simple formula for the computation of 2DS (in principle valid for any open quantum system described by a diagonalizable Liouvillian). As mentioned above, the density operator can be vectorized with a compact notation based on a single combined index. With this vectorized form, the time-dependent master equation reads $\frac{\mathrm{d}}{\mathrm{d}t}|\rho(t)\rangle\rangle = \hat{\mathcal{L}}|\rho(t)\rangle\rangle$. The formal solution is simply $|\rho(t)\rangle\rangle = e^{\hat{\mathcal{L}}t}|\rho(0)\rangle\rangle$, which can be straightforwardly represented within the basis of eigenstates $|v_i\rangle\rangle$ of the Liouvillian (with $\hat{\mathcal{L}}|v_i\rangle\rangle = \lambda_i|v_i\rangle\rangle$) as $|\rho(t)\rangle\rangle = \sum_i c_i^{(0)}e^{\lambda_i t}|v_i\rangle\rangle$, where $c_i^{(0)} = \langle\langle *|v_i\rangle\rangle\rho(0)$ are the coefficients of the initial density matrix in the Liouvillian eigenbasis. The matrix representation of the Liouvillian is neither Hermitian nor symmetric and the left and right eigenvectors are thus distinct, but do fulfill $\langle\langle *|v_i\rangle\rangle v_j = \delta_{ij}$.

Expressing the superoperator $(\breve{\mu}\hat{\rho} = \frac{1}{i\hbar}[\hat{\mu}, \hat{\rho}])$ in the eigenbasis of the field-free Liouvillian, $\breve{\mu}_{ij} = \langle\langle v_i|\breve{\mu}v_j\rangle\rangle$, then leads to a compact expression for the third-order density matrix. For instance, in the rephasing matching case, the result is

$$|\rho(t)\rangle\rangle = \sum_{ijkl} e^{\lambda_k t}e^{\lambda_j T}e^{\lambda_i \tau}\breve{\mu}^+_{kj}\breve{\mu}^+_{ji}\breve{\mu}^-_{il}c_l^{(0)}|v_k\rangle\rangle. \tag{16}$$

The field-free propagation during the times (t, T, τ) is reflected in the exponential factors.

The third-order nonlinear response function, $S = \mathrm{Tr}[\hat{\mu}^-\rho(t)]$, is obtained in Liouville space simply as $S = \langle\langle *|\hat{\mu}^+\rangle\rangle\rho(t)$. Thus, the expression for the rephasing response function becomes $S_R(\tau, T, t) = \sum_{ijkl} e^{\lambda_k t}e^{\lambda_j T}e^{\lambda_i \tau}\hat{\mu}^-_k\breve{\mu}^+_{kj}\breve{\mu}^+_{ji}\breve{\mu}^-_{il}c_l^{(0)}$, where $\hat{\mu}^-_k = \langle\langle *|\hat{\mu}^+\rangle\rangle v_k$. Performing a 2D Fourier transform over t and τ and reorganizing the summations then leads to a remarkably simple expression for the 2D spectrum:

$$S(\omega_t, T, \omega_\tau) = \sum_j E_j(\omega_\tau)e^{\lambda_j T}D_j(\omega_t), \tag{17}$$

with an excitation mask function $E_j = E_j^{NR} + E_j^R$, where

$$E_j^{NR/R}(\omega_\tau) = \sum_{il} \frac{1}{\pm i\omega_\tau + \lambda_i}\breve{\mu}^{\mp}_{ji}\breve{\mu}^{\pm}_{il}c_l^{(0)} \tag{18}$$

(the rephasing signal is located in the $(\omega_t, -\omega_\tau)$ quadrant [39]) and a detection mask function

$$D_j(\omega_t) = \sum_k \frac{1}{i\omega_t + \lambda_k}\hat{\mu}^-_k\breve{\mu}^+_{kj} \tag{19}$$

that only depend on excitation ω_τ and detection ω_t frequencies, respectively. Notice that the index j in Eq. 17 runs over the whole set of eigenstates of the Liouvillian. However, in practice, only a few of them contribute simultaneously to

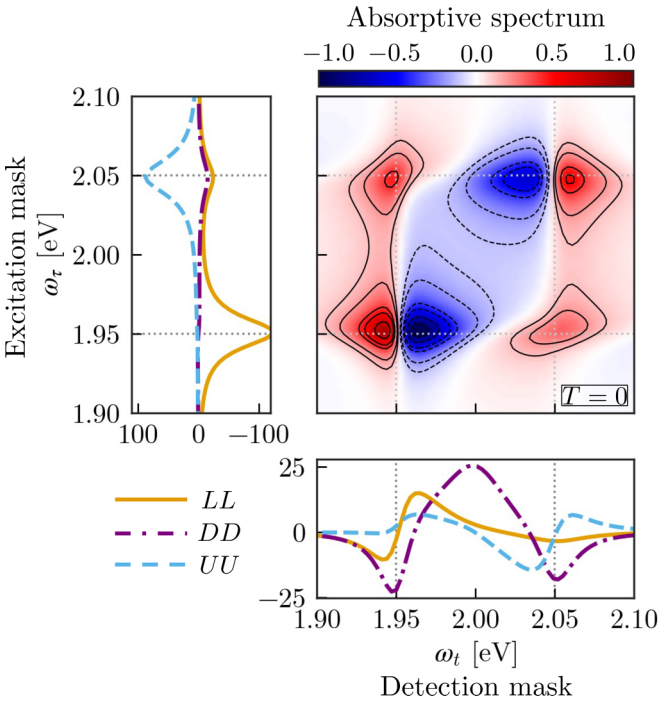

FIG. 5. 2D absorptive spectrum $S_{\mathrm{Abs}}(\omega_t, T, \omega_\tau)$ for a TC model with $N = 2$ molecules in resonance with the cavity $\omega_0 = \omega_c = 2$ eV, Rabi frequency $\Omega_R = 0.1$ eV, cavity lifetime 15 fs, and dephasing lifetime 50 fs, and BRW with a spectral function $J(\omega) = \gamma$ (at zero temperature) for waiting time $T = 0$. The spectrum is built following Eq. 17 with the index j running only over the three leading Liouvillian eigenvalues, that we label here as $\{\lambda_{LL}, \lambda_{UU}, \lambda_{DD}\}$ (see Fig. 2). The contributions to the excitation $\mathrm{Re}[E_j(\omega_\tau)]$ and detection $\mathrm{Re}[D_j(\omega_t)]$ masks are also plotted along the corresponding axis. 2D spectrum is normalized to unity at its maximum value.

the absorption and emission masks. We note that these mask functions are not directly observable quantities: the complex excitation mask $E_j(\omega_\tau)$ does not in general coincide with the linear absorption spectrum, and the complex detection mask $D_j(\omega_t)$ does not correspond to neither the emission spectrum nor any transient absorption spectrum.

An example of the construction of the 2DS through the excitation and detection mask functions is included in Fig. 5 (here and in the following, we set $\hbar = 1$). This plot corresponds to $\Re[S(\omega_t, T, \omega_\tau)]$ for a TC model with $N = 2$ molecular emitters with Rabi energy splitting $\Omega_R = 0.1$ eV subject to relaxation due to photon loss and dephasing, and for a chosen waiting time $T = 0$ so that the factor $e^{-\lambda_j T}$ is unity. In this particular case we find that from the 64 complex eigenvalues to be included in the sum in Eq. 17 (see also. Sec. II B), in practice we only need three eigenvalues (those corresponding to populations λ_{LL}, λ_{UU}, and λ_{DD}). In this case, even though the excitation mask barely shows a contribution from the dark state λ_{DD}, this becomes dominant in the detection mask and is responsible for the asymmetric signals at the cross peaks $(\omega_\tau, \omega_t) = (1.95, 2.05)$ eV and (2.05,1.95) eV. In contrast, this asymmetry between the two cross peaks is not present in the JC model (without dark states) at $T = 0$ (see Fig. 10 below).

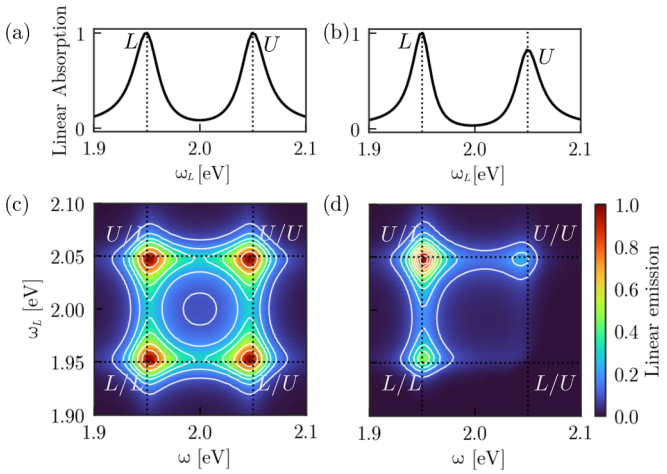

FIG. 6. (a) Linear absorption spectrum $S_{\mathrm{Abs}}(\omega_L)$ for a polariton system with $N = 2$ molecules within a resonant cavity $\omega_c = \omega_0 = 2$ eV with a Rabi splitting $\Omega_R = 0.1$ eV and cavity lifetime 15 fs and dephasing lifetime 50 fs. Absorption bands are located at $\omega_{LG} = 1.95$ eV and $\omega_{UG} = 2.05$ eV. Results obtained by using the Lindblad formalism for both cavity and molecular dephasing. (b) Same as (a) but using Bloch-Redfield-Wangsness theory, only for the molecular dephasing. (c) Excitation-emission spectrum $S_{\mathrm{Em}}(\omega_L, \omega)$ for the same polariton system as a function of the laser excitation frequency ω_L and emission frequency ω, using the Lindblad formalism. (d) Same as (c) but BRW theory replaces Lindblad formalism for dephasing. All spectra are normalized to unity at their respective maxima.

III. RESULTS

We have implemented the expressions above in a numerical code written in PYTHON and based on the QUTIP quantum optics toolbox [43], used to produce all results shown below. Due to the computational efficiency, all results presented in this work can be calculated on a desktop computer.

A. Linear spectroscopy

Upper (U) vs lower (L) polariton asymmetries in the signal strengths in both linear absorption and emission spectra of polaritons have already been analyzed theoretically [35,44], although in Ref. [44] using exclusively Lindblad operators. Instead, our approach using Markovian BRW theory introduces the asymmetry more naturally through the function $S_B(\omega)$ and provides a more consistent approach as implemented in Ref. [35] for absorption. In Fig. 6 we include the linear absorption and excitation-emission spectra for a TC model with $N = 2$ emitters. When the dephasing process is implemented as a Lindblad operator, both spectra are highly symmetrical. With the BRW theory the upper polariton absorbs less than the lower one and the emission spectra display a strong asymmetry where the U/L peak dominates. This reflects the importance of correctly representing the decay mechanisms of polaritons. In these linear spectroscopies, the states involved are the ground state G and those of the first excitation manifold $\{L, D, U\}$. The upper polariton U decays to the ground state G by photon loss but also to the lower polariton L and the dark states due to vibrational relaxation,

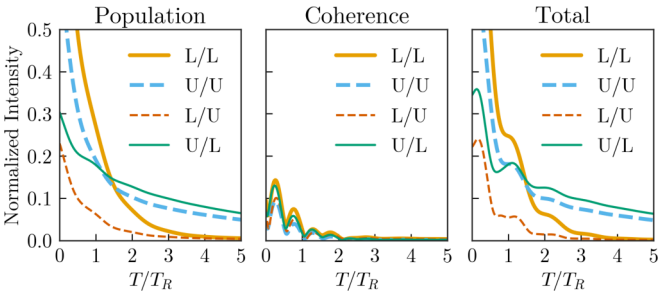

FIG. 7. Time evolution of the diagonal peaks {L/L,U/U} and cross peaks {L/U, U/L} in the two-dimensional spectrum $|S(\omega_t, T, \omega_\tau)|$ for a system of $N = 2$ molecules in resonance with the cavity $\omega_0 = \omega_c = 2$ eV, Rabi frequency $\Omega_R = 0.1$ eV, cavity lifetime 15 fs, and dephasing lifetime 50 fs. The chosen simple spectral density function here is $J(\omega) = \gamma$ at zero temperature. The components corresponding to populations (exponential) and coherences (oscillatory) are separated in the first two panels.

whereas the lower polariton decays only to the ground state (at low enough temperature or high enough Rabi splitting). Thus, the upper polariton peak is broadened in the absorption, and in the emission spectrum the path of laser excitation of the upper polariton followed by relaxation to the lower polariton produces the dominant U/L peak. However, these linear spectroscopies do not provide a detailed understanding on the inner dynamics of the polariton states involved, and below we study these emerging asymmetries beyond the linear response.

B. Non-linear 2D spectroscopy

In Sec. II E we derived a formula for the 2D spectral function $S(\omega_t, T, \omega_\tau)$ by which the 2DS at each pair of frequencies (ω_τ, ω_t) can be understood as built from the interference of damped oscillations, $e^{\lambda_j T} = e^{-\Gamma_j T} e^{i\omega_j T}$, with different amplitudes $E_j(\omega_\tau)D_j(\omega_t)$. A detailed analysis reveals that only for a few Liouvillian eigenstates neither the excitation nor the detection mask functions vanish, and only these contribute to the sum over j in Eq. 17. In our polariton showcase, these states are related to Hamiltonian populations $\{LL, UU, DD\}$ and coherences $\{LU, UL\}$. The temporal factor $e^{-\Gamma_j T}$ causes a leading exponential decay during the waiting time T, while the factor $e^{i\omega_j T}$ explains the ubiquitous presence of Rabi oscillations in the 2DS, since the only contributing frequencies $\omega_j \sim \pm\omega_{UL}$ correspond to coherences that involve the lower L and upper U polaritons (see Fig. 7 where we illustrate the crucial importance of coherences during the waiting time T since they provide most of the oscillatory components). As analyzed in the theory Sec. II B, the location of the eigenvalues in the complex plane helps to understand the relative global decay of populations, showing that the upper polariton decays faster because it has three available decay channels ($U \to G$ due to photon loss and $U \to D$ and $U \to L$ due to vibrational bath relaxation). Both the lower polariton and the dark states have a single decay channel each ($L \to G$ due to photon loss and $D \to L$ due to vibrational relaxation). In many experimental implementations with thin metallic mirrors, photon loss lifetimes are shorter than molecular dephasing lifetimes [4], and we here choose 15 fs for $1/\kappa$ and 50 fs for $1/\gamma$. However, note that for the comparison of our results with the experimental ones of Ref. [23] in Sec. III C, the reverse criterion ($1/\kappa > 1/\gamma$) is required for improved agreement.

For the open TC systems, a major feature is found in the computed 2DS as the waiting time T increases (see Fig. 7); they develop strong asymmetries during the waiting time T, revealed by the relative intensities of cross peaks ($L/U < U/L$), with the diagonal peak L/L displaying the fastest decay (see Fig. 7). A similar behavior is found experimentally for J-aggregates within optical cavities [23], as discussed below. In contrast, for a nondissipative TC model the 2DS shows identical diagonal peak intensities (L/L and U/U) in temporal counterphase with identical cross-peak heights (U/L and L/U) for all waiting times T and the 2DS show full revivals when T/T_R is integer (Rabi oscillations).

To understand the origin of these asymmetries in 2DS, in Fig. 8 we analyze the calculation step by step for a dissipative TC model with $N = 2$. Intermediate temporal expressions for the density $|\rho\rangle\rangle$ help us to track the history at each step. Note that the perturbative density matrix $\rho(t)$ is not Hermitian and is not represented by a positive definite matrix, since $\rho^{(3)}$ for a given phase-matching condition involves commutators with non-Hermitian coupling interactions $\hat{\mu}^+$ and $\hat{\mu}^-$.

(1) The first pulse takes the ground-state population GG to the coherences $\{GL, GU\}$ [rephasing case, see Fig. 4(b)] and $\{LG, UG\}$ (nonrephasing). These coherences form independent diagonal blocks in the Liovillian representation and do not mix.

(2) Time evolution τ: the coherences evolve within their matrix blocks with a phase $e^{\lambda_j \tau}$, where λ_j contains frequencies $\omega_j \sim \pm\omega_{GU}$ or $\omega_j \sim \pm\omega_{GL}$, so that signals in the 2DS are expected at both frequencies. From the Liouvillian master equations we extract $\dot{\rho}_{LG} = -(\kappa/2)\rho_{LG} + (\gamma/8 - \kappa/2)\rho_{UG}$ and $\dot{\rho}_{UG} = -(\kappa/2)\rho_{LG} + (-\gamma/8 - \kappa/2)\rho_{UG}$. Thus, the dephasing (with the parameter γ) makes the coherence UG decay slightly faster than the LG one.

(3) The second pulse takes the previous coherences to populations $\{GG, LL, UU\}$ and coherences $\{LU, UL\}$ (contained in another diagonal block in the Liouvillian matrix). The Fourier transform of $\Re[\rho(t)]$ up to this step is plotted in Fig. 8(a). Whereas the population LL inherits a combination $\propto -(LG - GL)$ from step 2 (and consequently produces a signal at frequency $\omega_\tau = \omega_{LG}$ but zero at ω_{UG}), the population UU comes from $\propto -(UG + GU)$ (with a peak at frequency $\omega_\tau = \omega_{UG}$ but zero at ω_{LG}). Therefore, both signals must be asymmetric with respect to frequencies ω_{LG} and ω_{UG}. The GG population results from the combination $\propto +(UG - LG + GL - GU)$ that carries both frequencies (almost yields a symmetric signal) and has opposite sign with respect to the other populations. A similar reasoning follows for the coherences LU and UL. Since the coherence UG decays faster during the evolution with τ, the peaks at $\omega_\tau = \omega_{UG}$ show a lower intensity here.

(4) Evolution during T. In Fig. 8(b), we show two different waiting times. For small times, $T/T_R = 0.5$, the appearance of the dark state population DD and the sign inversion of the coherences $\{LU, UL\}$ can already be noticed. At longer times, $T/T_R = 5.0$, the populations decay at ω_{LG}, but those of the ground and dark states prevail at ω_{UG}. Here, it can be appreciated that the ground-state population increases roughly with the exponential decay of lower

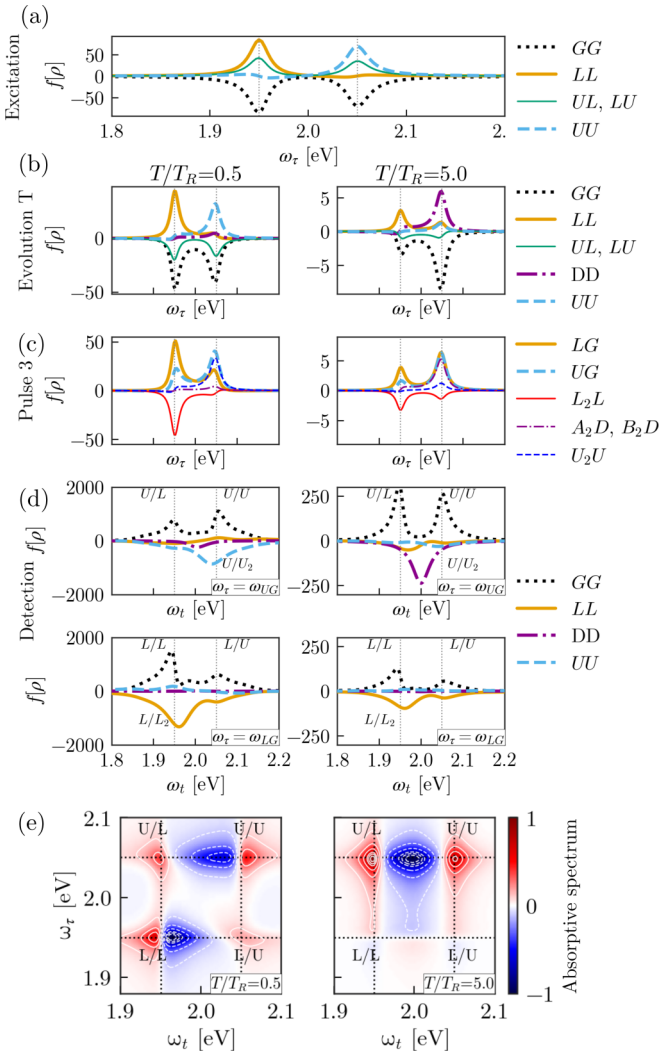

FIG. 8. Temporal buildup of the 2DS for a TC model with $N = 2$ in a vertical timeline with four stages: (a) excitation [pulse 1, τ, pulse 2], (b) waiting T, (c) pulse 3, and (d) detection. In the figures $f(\rho)$ indicates the Fourier transform of Re$[\rho(t)]$ for the rephasing plus nonrephasing contributions. Solid lines indicate the nonzero components of $f(\rho)$ in terms of the Hamiltonian eigenstates in the three excitation manifolds Λ_0, Λ_1, and Λ_2. Vertical dashed lines indicate the positions of the transition frequencies $\omega_{LG} = 1.95$ eV and $\omega_{UG} = 2.05$ eV. Two waiting times are considered, $T/T_R = 0.5$ and $T/T_R = 5.0$. At the detection stage, $f(\rho)$ is plotted against ω_t and the solid line of the component G-G corresponds exactly to the 2DS along the cuts $\omega_\tau = \omega_{LG}$ and $\omega_\tau = \omega_{UG}$. (e) 2DS absorptive spectrum $S_{\rm Abs}(\omega_t, T, \omega_\tau)$ for the two waiting times. The system and parameters for this calculation are the same as described in Fig. 7. Spectra are normalized to unity at their maxima.

polariton population LL, at ω_{LG}. In contrast, at ω_{UG} the ground-state population increases due to the upper polariton U decay, but to a lesser extent also because U decays into the dark state D. This is in fact the crucial step due to which the L vs U asymmetry eventually appears in the 2DS.

(5) Pulse 3 causes the transfer to the coherence blocks $\{LG, UG\}$ and $\{\Lambda_2\Lambda_1\}$. From the previous step, $\{GG, LL, LU\}$ contribute to the coherence LG and $\{GG, UL, UU\}$ do so for the coherence UG. This explains the components seen in Fig. 3(c). Specifically, for long waiting times the shapes of $\{LG, UG\}$ coherences originate from the dominant ground state in Fig. 8(b). Also, population DD is excited to coherences $\Lambda_2 D$. Similarly, LL transfers to L_2L and UU to U_2U.

(6) Signal is detected during the evolution in time t: the coherences $\{LG, UG\}$ decay to the ground-state population GG and coherences $\{\Lambda_2 L, \Lambda_2 U, \Lambda_2 D\}$ decay radiatively to the Λ_1 populations LL, DD, and UU, plotted in Fig. 8(d) along the excitation cuts $\omega_\tau = \omega_{UG}$ and $\omega_\tau = \omega_{LG}$. The sum of these populations gives the structures observed in the 2DS in Fig. 8(e).

When exciting at the upper polariton frequency $\omega_\tau = \omega_{UG}$, the most important negative contribution to the 2DS comes from the population UU at short waiting times, whereas at long waiting times the U state decays into the dark states and the DD population dominates. In contrast, for lower polariton excitation $\omega_\tau = \omega_{LG}$, the dynamics of the negative contribution to the 2DS is governed by the LL population at any waiting time, because dark states hardly contribute to the dynamics and all populations have similar shapes during T (only the intensity is reduced exponentially as expected). Whereas the population contributions tend to approximately cancel each other for lower polariton excitation as T increases, this does not occur when pumping the upper polariton, which has a different mechanism that is contributed by the dark state. Ultimately, this explains why at long waiting times the U/L and U/U peaks remain visible against the more rapidly vanishing L/L and L/U peaks in the 2DS.

To understand these asymmetries in another way, we show in Fig. 9 the decomposition of the total 2DS of Fig. 8(e) into all Feynman path components GSB, GSR, SE, ESA, and ESA′ for the same two waiting times. The GSB positive contribution remains constant during the waiting time, while GSR grows (with opposite sign) since any state finally decays into the ground state. For long waiting times the LL population fully relaxes by photon loss after excitation into the ground state and GSR roughly produces the same signal as the GSB component but with opposite sign, thus producing a complete cancellation in the spectra at $\omega_\tau = \omega_{LG}$ (lower peaks L/L and L/U). At variance, the UU population may decay by dephasing relaxation to the dark D state and lower L state, and to the ground state by photon loss. Thus, the residual GG population to be excited by the third pulse in GSR becomes smaller than in GSB, which leads to only a partial cancellation in GSB + GSR at the upper peaks U/L and U/U. In the negative ESA component, the third pulse makes the difference when exciting at $\omega_\tau = \omega_{LG}$ or $\omega_\tau = \omega_{UG}$. In the former case, the coherence L_2L moves back to the LL population in detection, aided only by a cavity photon loss; in the latter case the coherence U_2U decays into UU and subsequently into DD populations at detection, aided by both molecular relaxation and cavity photon loss. Eventually, the DD population produces the remnant ESA signal, already present for $T/T_R = 5.0$.

The contribution of the five different components (GSB, SE, ESA, GSR, and ESA′) to the 2DS depends upon the waiting time T. In this respect both components SE and ESA′ are crucial in the construction of the full 2DS but they tend to vanish at large waiting times due to the relaxation of

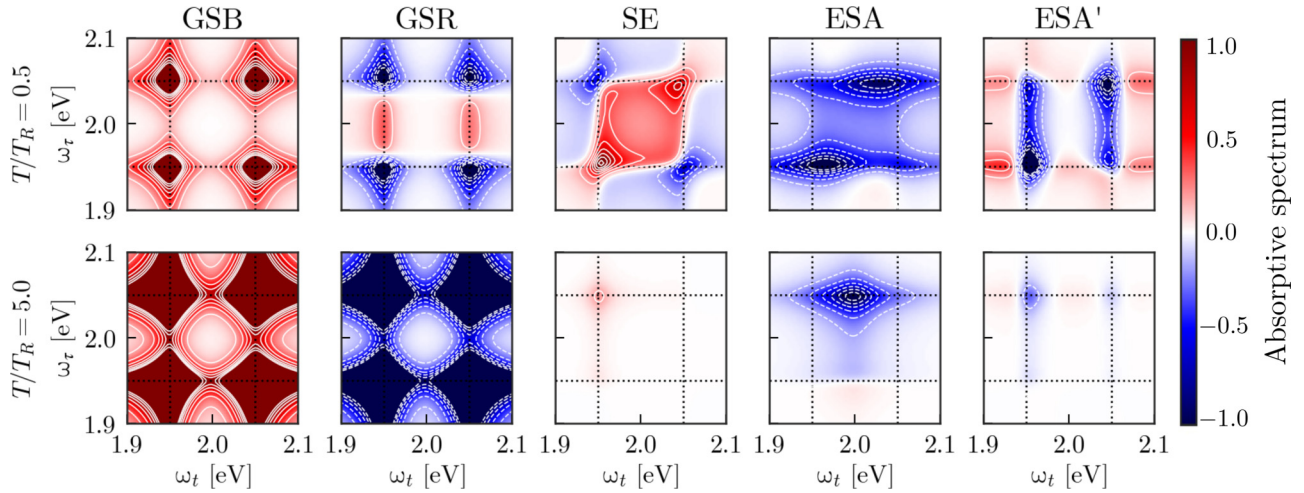

FIG. 9. Components GSB, GSR, SE, ESA, and ESA′ of the total absorptive spectrum $S_{\mathrm{Abs}}(\omega_t, T, \omega_\tau)$ plotted in Fig. 8(e) for two different waiting times $T/T_R = 0.5$ and $T/T_R = 5.0$, related to the Feynman paths quoted in Fig. 4(b). Each component contributes to a total absorptive spectrum which is normalized to unity at its maximum. It is worth noting that 2D plots always contain both population and coherence components, so that GSR and SE show both positive and negative signals at short T. At large T GSR is negative and it compensates the positive GSB and the residual SE becomes positive.

populations and coherences from the Λ_1 and Λ_2 excitation manifolds. The mechanism of the ESA′ component corresponds to relaxation between coherences of different excitation manifolds from $|\Lambda_2\rangle\langle\Lambda_1|$ to $|\Lambda_1\rangle\langle G|$. In Fig. 9 both contributions ESA and ESA′ clearly contribute to the negative part of the spectrum at short waiting time, $T/T_R = 0.5$, while SE and ESA′ components tend to vanish for the positive and negative part of the spectra, respectively, for $T/T_R = 5$ and ESA remains the main negative contribution.

In addition to the case with $N = 2$ molecules discussed above, we have also studied the 2DS for $N = 1$ (Jaynes-Cummings) and for $N = 3$ and $N = 10$. Concerning the case $N = 1$ we do not observe the same fading trends at large T in the 2DS (see Fig. 10). In the absence of a dark state, here the upper polariton still has two decay mechanisms (radiative $U \to G$ and vibrational $U \to L$) so that at long T the GSR signal for excitation at $\omega_\tau = \omega_{UG}$ should be larger than for excitation at $\omega_\tau = \omega_{LG}$. However, this difference is very small compared with the case $N > 1$ with dark states. As T increases, the GSR signals at any of the peaks fully cancel the constant GSB, and this happens almost simultaneously. Additionally, a shift of the peak energy of the negative ESA components is visible along the excitation cut $\omega_\tau = \omega_{UG}$ during T. At short time T, the ESA peak is centered at the $U_2 \to U$ transition. However, due to the dissipative $U \to L$ decay, for large T the third pulse mainly excites the L state to the second excitation manifold, with the subsequent ESA peak centered at the transition $L_2 \to L$.

For the case of $N > 2$, as N increases, the energies of states $\{A_2\}$ and $\{B_2\}$ in Λ_2 get closer to those of the L_2 and U_2 polaritons, respectively. Thus, the ESA contributions for $N > 2$ produce negative signals approaching the detection frequencies $\omega_\tau = \omega_{LG}$ and $\omega_\tau = \omega_{UG}$ (see Fig. 10). Note also that these states in Λ_2 are radiatively connected to the $N - 1$ dark states in Λ_1. However, the mechanism involving the collection

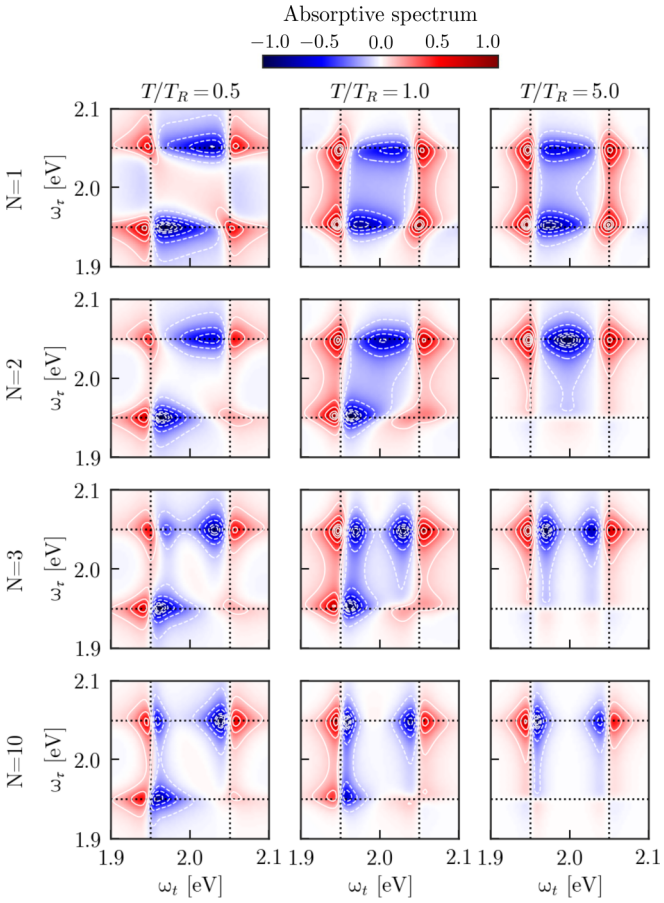

FIG. 10. 2DS for the dissipative Tavis-Cummings system for a different number of molecules $N = 1, 2, 3$, and 10, and for three different waiting times $T/T_R = 0.5$, 1.0, and 5.0. The parameters are the same as quoted in Fig. 9. All 2DS are normalized to unity at their maxima.

of dark states remains unaltered and the conclusions reached for $N = 2$ are also valid for large N. Our results indicate that the shape of 2DS remains unchanged for $N \geqslant 3$, while the global intensity reduces with increasing N. In the thermodynamic limit $N \to \infty$, the TC model becomes linear and can be represented by two coupled harmonic oscillators [22], such that the anharmonicity that leads to a nonzero 2DS disappears. However, a realistic treatment of 2DS for large systems would require going beyond the third-order perturbative limit, as the number of absorbed photons would also increase with N for a given driving strength [37], reaching much higher excitation manifolds Λ_n, with the nonlinearity scaling as n/N. The system is then expected to behave similarly as a TC model with a small number of molecules, as implied by the reasonable agreement with experiments (see Fig. 11 below).

C. Comparison with experiments

Recent experiments with a polaritonic system involving molecular J-aggregates [23] inside a microcavity show three main features in 2DS as a function of increasing waiting time T (see Fig. 11), namely,

(1) the 2DS rapidly develops an asymmetry where the U/L cross peak gains in intensity, while the L/U cross peak disappears;

(2) the diagonal peak L/L, initially the most intense, has the fastest decay and drops to an intensity level comparable to the U/L cross peak; and

(3) the peaks L/L and U/L dominate compared to the U/U and L/U peaks.

To reproduce these features, we study a dissipative TC model with $N = 5$ molecules (larger ensembles do not show distinguishable differences in the 2DS, as discussed above) with a two-level natural frequency $\omega_e = 2.09$ eV and with a slightly blue-shifted cavity mode, $\omega_c = 2.1$ eV. As in the experiment, the Rabi frequency is chosen as $\Omega_R = 0.3$ eV. To reproduce the experimental conditions more realistically, temperature effects are also incorporated in the exciton-phonon coupling through a Debye spectral function for the bath at room temperature $T = 300$ K and using a frequency cut-off parameter $\delta = 0.2$ eV. We also find that the cavity lifetime (120 fs) must be set somewhat longer than the dephasing lifetime (60 fs) to reproduce the three experimental features listed above. The source of these phenomena stems from the relaxation mechanisms of states in Λ_1 and Λ_2 manifolds as explained above. Of course, the comparison of the simple model treated here with the experiment is not perfect. J-aggregates have interactions with the environment and between molecules in addition to a phonon structure that might cause a slower decay of peaks than that produced by the electronic motion alone. Oscillations in the L/L and U/L peaks vs T present in the experiment below 500 fs [Fig. 11(c)] cannot be attributed to electronic Rabi oscillations [which, in fact, are much faster and visible in the theoretical peaks L/U and U/L below 500 fs in Fig. 11(b)]. We speculate that a more detailed account of the vibrational structure and its influence on the polariton modes (in the current model determined by the single parameter γ) would be required to reproduce these experimental features while keeping a shorter cavity lifetime. However, despite the simplicity of our model, the

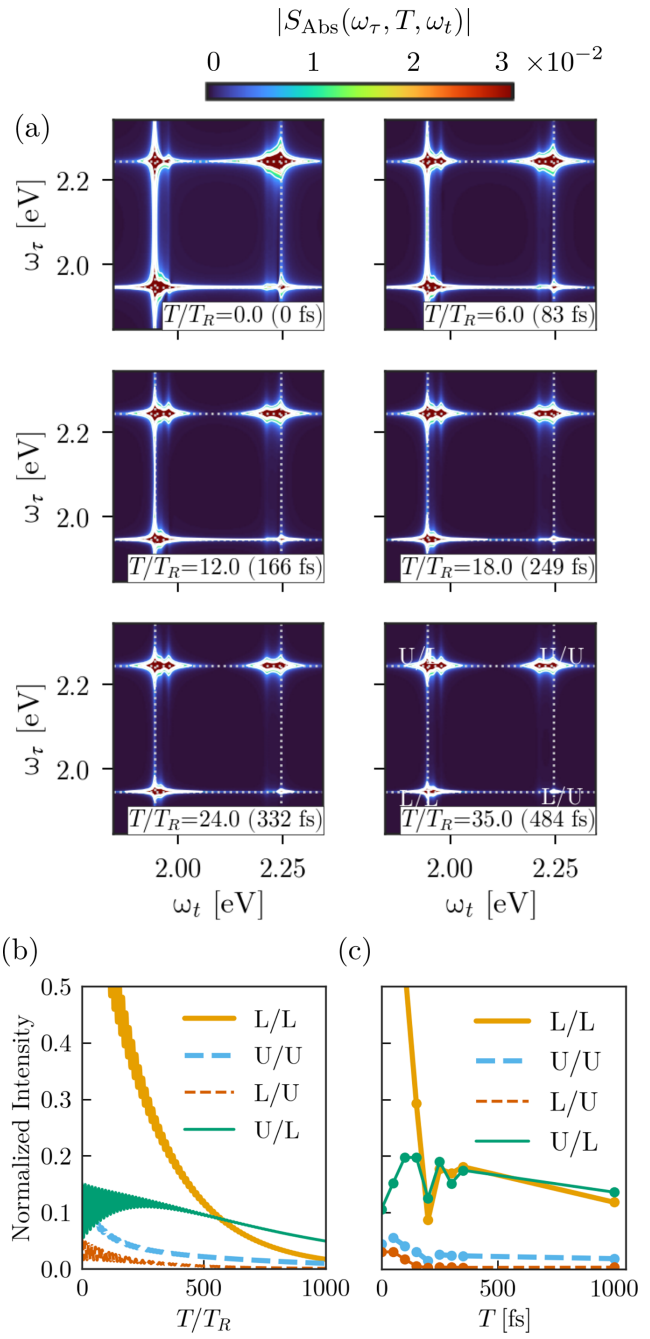

FIG. 11. (a) 2DS $|S(\omega_t, T, \omega_\tau)|$ for a TC model with $N = 5$ emitters, for different waiting times T (in units of the Rabi period $T_R = 1/\Omega_R = 13.8$ fs). The 2DS at waiting time $T/T_R = 0$ is normalized to unity at its maximum value and those for $T/T_R > 0$ share the same scale as in $T/T_R = 0$. The molecular system has a small positive detuning with $\omega_c = 2.1$ eV and $\omega_0 = 2.09$ eV, and a Rabi splitting $\Omega_R = 0.3$ eV. Dotted lines indicate the positions for the transition frequencies $\omega_{LG} = 1.945$ eV and $\omega_{UG} = 2.245$ eV. Cavity lifetime is 120 fs and molecular dephasing lifetime is chosen as 60 fs, and we have also considered a Debye spectral function (with cut-off $\delta = 0.2$ eV) at room temperature ($T = 300$ K). (b) Time evolution of the diagonal- and cross-peak maxima in (a) in terms of the waiting time T. The peak heights are renormalized such that the value of the highest peak L/L at $T = 0$ is unity. (c) Experimental data extracted from diagonal and cross peaks in the 2DS in Ref. [23] corresponding to a system of J-aggregates within an optical cavity.

reproduction of the trends of these three experimental features is remarkable.

It would be useful to extract from the experimental 2DS some physical parameters, such as partial decay rates for the processes involved in the polariton photodynamics. The time evolution of diagonal or cross peaks against the waiting time already contains information on the decays. From our expression for 2DS Eq. 17 we can extract the value of the spectra at any frequency point (ω_τ, ω_t). For the L/L diagonal peak the analytical expression for the peak intensity reads

$$\begin{aligned}|S(\omega_L, T, \omega_L)|^2 &= C_1 e^{-2\Gamma_{LL}T} + e^{-(\Gamma_{LL}+\Gamma_{UL})T} \\ &\times [C_2 \cos(\Omega_R T) + C_3 \sin(\Omega_R T)] + e^{-2\Gamma_{UL}T} \\ &\times [C_4 \cos^2(\Omega_R T) + C_5 \sin^2(\Omega_R T) + C_6 \sin(2\Omega_R T)],\end{aligned} \tag{20}$$

where $\Gamma_{LL} = \kappa/2$ and $\Gamma_{UL} = \kappa/2 + \gamma/8$. From the latter equation we have worked out a simplified expression to fit the 2DS L/L peak,

$$\begin{aligned}|S(\omega_L, T, \omega_L)|^2 \sim |A e^{-2\Gamma_{LL}T} + e^{-2\Gamma_{UL}T} [B \cos(\Omega_R T) \\ + C \sin(\Omega_R T)]|.\end{aligned} \tag{21}$$

For instance, for the 2DS obtained for the JC model in Fig. 10, using $\kappa = 0.044$ eV (lifetime 15 fs) for cavity photon loss and $\gamma = 0.0132$ (lifetime 50 fs) for dephasing, the fitting of the L/L peak against T with this five-parameter function $(A, B, C, \kappa, \gamma)$ (Rabi frequency Ω_R is extracted directly from the oscillations in the plot) yields 15 and 43 fs, respectively.

IV. CONCLUSIONS

In this work, we have analyzed the structure and dynamics of cavity polaritons derived from fundamental models such as Jaynes-Cummings and Tavis-Cummings Hamiltonians combined with a perturbative treatment of exciton-vibration interactions in order to understand the outcome of multidimensional coherent spectroscopy when applied to molecules. We have derived an efficient pseudo-analytic procedure to compute 2DS for three nonoverlapping laser pulses that allows to interpret the two-dimensional spectrum by analyzing their buildup at any stage, namely, excitation, evolution, probe, and detection.

Asymmetries in experimental 2DS concerning diagonal and cross peaks are here explained by the crucial role played by dark states within the first excitation manifold. We show the relevance of components GSR and ESA′ that involve relaxation in addition to the standard GSB, SE, and ESA components. The dynamic role of coherences is to bring oscillatory patterns to the spectra, on top of the background contributed by populations, and is clearly relevant during the waiting time between pump and probe. Finally, some emerging features in the ESA path produce a directly detected signal in the 2DS that conforms a fingerprint of dark states.

The 2D experimental spectra with J-aggregates has more complex structures and features that cannot be reproduced fairly with our simplified model. Further developments require to include molecular vibrational states with their corresponding anharmonicity, disorder, and broadening effects that eventually contribute at longer waiting times beyond the fast electronic photodynamics. Also, we think our method and conclusions may find applications in other scenarios, for instance, in semiconductor microcavities [45] or to understand relaxation in plexcitonic materials [46]. We hope this work may contribute to the design of new experiments with electronic polaritons involving molecular ensembles in microcavities, with emphasis on preparing the active system with just a few atoms or molecules, which by itself is quite an experimental challenge.

ACKNOWLEDGMENTS

We acknowledge funding by the Vicerrectoría de Investigación at Universidad de Antioquia under Project No. CODI Programática 2022-53576, by the Spanish Ministry for Science and Innovation-Agencia Estatal de Investigación (AEI) through Grants No. PID2021-125894NB-I00 and No. CEX2018-000805-M (through the María de Maeztu program for Units of Excellence in R&D), and by the European Research Council through Grant No. ERC-2016-StG-714870. L.M. acknowledges the Swiss National Science Foundation, Project No. P2ELP2_187957.

[1] F. Herrera and F. C. Spano, Cavity-controlled chemistry in molecular ensembles, Phys. Rev. Lett. **116**, 238301 (2016).

[2] R. F. Ribeiro, L. A. Martínez-Martínez, M. Du, J. Campos-Gonzalez-Angulo, and J. Yuen-Zhou, Polariton chemistry: Controlling molecular dynamics with optical cavities, Chem. Sci. **9**, 6325 (2018).

[3] J. Feist, J. Galego, and F. J. Garcia-Vidal, Polaritonic chemistry with organic molecules, ACS Photonics **5**, 205 (2018).

[4] J. Fregoni, F. J. Garcia-Vidal, and J. Feist, Theoretical challenges in polaritonic chemistry, ACS Photonics **9**, 1096 (2022).

[5] S. Mukamel, Multidimensional femtosecond correlation spectroscopies of electronic and vibrational excitations, Annu. Rev. Phys. Chem. **51**, 691 (2000).

[6] D. M. Jonas, Two-dimensional femtosecond spectroscopy, Annu. Rev. Phys. Chem. **54**, 425 (2003).

[7] D. Abramavicius, B. Palmieri, D. V. Voronine, F. Sanda, and S. Mukamel, Coherent multidimensional optical spectroscopy of excitons in molecular aggregates; quasiparticle versus supermolecule perspectives, Chem. Rev. **109**, 2350 (2009).

[8] F. D. Fuller and J. P. Ogilvie, Experimental implementations of two-dimensional Fourier transform electronic spectroscopy, Annu. Rev. Phys. Chem. **66**, 667 (2015).

[9] P. Saurabh and S. Mukamel, Two-dimensional infrared spectroscopy of vibrational polaritons of molecules in an optical cavity, J. Chem. Phys. **144**, 124115 (2016).

[10] K. E. Dorfman and S. Mukamel, Multidimensional photon correlation spectroscopy of cavity polaritons, Proc. Natl. Acad. Sci. **115**, 1451 (2018).

[11] V. Tiwari, Multidimensional electronic spectroscopy in high-definition—Combining spectral, temporal, and spatial resolutions, J. Chem. Phys. **154**, 230901 (2021).

[12] T. A. A. Oliver, Recent advances in multidimensional ultrafast spectroscopy, R. Soc. Open Sci. **5**, 171425 (2018).

[13] A. Gelzinis, R. Augulis, V. Butkus, B. Robert, and L. Valkunas, Two-dimensional spectroscopy for non-specialists, Biochim. Biophys. Acta, Bioenerg. **1860**, 271 (2019).

[14] R. F. Ribeiro, A. D. Dunkelberger, B. Xiang, W. Xiong, B. S. Simpkins, J. C. Owrutsky, and J. Yuen-Zhou, Theory for nonlinear spectroscopy of vibrational polaritons, J. Phys. Chem. Lett. **9**, 3766 (2018).

[15] B. Xiang, R. F. Ribeiro, A. D. Dunkelberger, J. Wang, Y. Li, B. S. Simpkins, J. C. Owrutsky, J. Yuen-Zhou, and W. Xiong, Two-dimensional infrared spectroscopy of vibrational polaritons, Proc. Natl. Acad. Sci. **115**, 4845 (2018).

[16] B. S. Simpkins, Z. Yang, A. D. Dunkelberger, I. Vurgaftman, J. C. Owrutsky, and W. Xiong, Comment on "isolating polaritonic 2D-IR transmission spectra", J. Phys. Chem. Lett. **14**, 983 (2023).

[17] H. Li and S. T. Cundiff, Chapter One – 2D coherent spectroscopy of electronic transitions, in *Advances In Atomic, Molecular, and Optical Physics*, edited by E. Arimondo, C. C. Lin, and S. F. Yelin (Academic, New York, 2017), Vol. 66, p. 1.

[18] E. T. Jaynes and F. W. Cummings, Comparison of quantum and semiclassical radiation theories with application to the beam maser, Proc. IEEE **51**, 89 (1963).

[19] B. W. Shore and P. L. Knight, The Jaynes-Cummings model, J. Mod. Opt. **40**, 1195 (1993).

[20] R. Dicke, Coherence in spontaneous radiation processes, Phys. Rev. **93**, 99 (1954).

[21] M. Tavis and F. W. Cummings, Exact solution for an N-molecule-radiation-field Hamiltonian, Phys. Rev. **170**, 379 (1968).

[22] B. M. Garraway, The Dicke model in quantum optics: Dicke model revisited, Philos. Trans. R. Soc. London A **369**, 1137 (2011).

[23] L. Mewes, M. Wang, R. A. Ingle, K. Börjesson, and M. Chergui, Energy relaxation pathways between light-matter states revealed by coherent two-dimensional spectroscopy, Commun. Phys. **3**, 157 (2020).

[24] M. Kasha, Energy transfer mechanisms and the molecular exciton model for molecular aggregates, Radiat. Res. **20**, 55 (1963).

[25] N. J. Hestand and F. C. Spano, Expanded theory of H- and J-molecular aggregates: The effects of vibronic coupling and intermolecular charge transfer, Chem. Rev. **118**, 7069 (2018).

[26] F. Fassioli, K. H. Park, S. E. Bard, and G. D. Scholes, Femtosecond photophysics of molecular polaritons, J. Phys. Chem. Lett. **12**, 11444 (2021).

[27] Z. Zhang, K. Wang, Z. Yi, M. S. Zubairy, M. O. Scully, and S. Mukamel, Polariton-assisted cooperativity of molecules in microcavities monitored by two-dimensional infrared spectroscopy, J. Phys. Chem. Lett. **10**, 4448 (2019).

[28] M. E. Mondal, E. R. Koessler, J. Provazza, A. N. Vamivakas, S. T. Cundiff, T. D. Krauss, and P. Huo, Quantum dynamics simulations of the 2D spectroscopy for exciton polaritons, J. Chem. Phys. **159**, 094102 (2023).

[29] Z. Zhang, X. Nie, D. Lei, and S. Mukamel, Multidimensional coherent spectroscopy of molecular polaritons: Langevin approach, Phys. Rev. Lett. **130**, 103001 (2023).

[30] M. Sánchez-Barquilla, A. I. Fernández-Domínguez, J. Feist, and F. J. García-Vidal, A theoretical perspective on molecular polaritonics, ACS Photonics **9**, 1830 (2022).

[31] H.-P. Breuer *et al.*, *The Theory of Open Quantum Systems* (Oxford University, New York, 2002).

[32] J. Jeske and J. H. Cole, Derivation of Markovian master equations for spatially correlated decoherence, Phys. Rev. A **87**, 052138 (2013).

[33] D. Manzano, A short introduction to the Lindblad master equation, AIP Adv. **10**, 025106 (2020).

[34] J. Jeske, D. J. Ing, M. B. Plenio, S. F. Huelga, and J. H. Cole, Bloch-Redfield equations for modeling light-harvesting complexes, J. Chem. Phys. **142**, 064104 (2015).

[35] J. del Pino, J. Feist, and F. J. Garcia-Vidal, Quantum theory of collective strong coupling of molecular vibrations with a microcavity mode, New J. Phys. **17**, 053040 (2015).

[36] D. Lentrodt and J. Evers, Ab initio few-mode theory for quantum potential scattering problems, Phys. Rev. X **10**, 011008 (2020).

[37] S. Mukamel, *Principles of Nonlinear Optical Spectroscopy* (Oxford University, New York, 1999).

[38] M. Cho, *Two-Dimensional Optical Spectroscopy* (CRC Press, Boca Raton, 2009).

[39] P. Hamm and M. Zanni, *Concepts and Methods of 2D Infrared Spectroscopy* (Cambridge University, Cambridge, 2011).

[40] M. F. Gelin, D. Egorova, and W. Domcke, Efficient calculation of time-and frequency-resolved four-wave-mixing signals, Acc. Chem. Res. **42**, 1290 (2009).

[41] A. De Sio, X. T. Nguyen, and C. Lienau, Signatures of strong vibronic coupling mediating coherent charge transfer in two-dimensional electronic spectroscopy, Z. Naturforsch. A **74**, 721 (2019).

[42] L. Valkunas, D. Abramavicious, and T. Mančal, *Molecular Excitation Dynamics* (Wiley, New York, 2013).

[43] J. Johansson, P. Nation, and F. Nori, QuTiP 2: A Python framework for the dynamics of open quantum systems, Comput. Phys. Commun. **184**, 1234 (2013).

[44] T. Neuman and J. Aizpurua, Origin of the asymmetric light emission from molecular exciton–polaritons, Optica **5**, 1247 (2018).

[45] N. Takemura, S. Trebaol, M. D. Anderson, V. Kohnle, Y. Léger, D. Y. Oberli, M. T. Portella-Oberli, and B. Deveaud, Two-dimensional fourier transform spectroscopy of exciton-polaritons and their interactions, Phys. Rev. B **92**, 125415 (2015).

[46] D. Finkelstein-Shapiro, P.-A. Mante, S. Sarisozen, L. Wittenbecher, I. Minda, S. Balci, T. Pullerits, and D. Zigmantas, Understanding radiative transitions and relaxation pathways in plexcitons, Chem **7**, 1092 (2021).